Characterization of Himawari-8 AHI 3.9 μm Channel Stray Light

Xi Shao[1,2], Xiangqian Wu[3], Fangfang Yu[1]

[1]Earth Resource Technology, Inc., Laurel, MD, USA
[2] University of Maryland, College Park, MD, USA
[3]NOAA/NESDIS/STAR, College Park, MD, USA

ABSTRACT

The Advanced Himawari Imager (AHI) is the primary instrument aboard Himawari-8 and has 16 multispectral channels, including six visible and near infrared and 10 thermal emissive bands. The 3.9-μm channel imagery of AHI has spatial resolution of 2 km and performs routine full-disk imaging every 10 minutes. There have been stray light observed in the full disk imagery of the AHI 3.9-μm channel over a few weeks around February and October-November when the line of sight of the sun is at ~10 to ~20 degrees south of the nadir of the Himawari-8. In this paper, difference data between consecutive AHI 3.9-μm images have been processed to quantitatively characterize and monitor the AHI stray light. Stray light indices are also developed to trend the occurrence, position and magnitude of the stray light in the AHI 3.9-μm imageries. It is also found that the stray light is the greatest in the AHI 3.9-μm band but also is detectable in other Mid-Wavelength IR channels. Analysis of the ratio of stray light magnitude between AHI 3.9-μm and 6.2-μm band indicates that it is consistent with the ratio of solar radiance for these two bands. This suggests that the stray light is mainly due to direct illumination of the attenuated solar radiation on the AHI detector rather than from onboard thermal body emission due to heating. The upcoming Advanced Baseline Imager (ABI) onboard the GOES-R satellite has very similar spectral and spatial characteristics as AHI. Therefore, characterizing the stray light in the 3.9-μm channel of AHI helps support post-launch calibration activities of ABI.

Keywords: Himawari-8, Advanced Himawari Imager, AHI, GOES-R ABI, MWIR Calibration, Stray light

1. INTRODUCTION

The Himawari-8 is the eighth Japanese geostationary weather satellites operated by the Japan Meteorological Agency and was successfully launched on October 7, 2014 [1-7]. Himawari-8 is in operation around 140.7 degrees East longitude covering the East Asia and Western Pacific regions. The Advanced Himawari Imager (AHI) is the primary instrument aboard Himawari-8. It has 16 multispectral channels, including six visible and near infrared (VNIR) and 10 thermal emissive bands (TEBs). The new design of the AHI including double scan mirrors and controlled calibration target temperature improves the radiometric accuracy of the TEBs. Two scanning mirrors of AHI control the East/West (E/W) and North/South (N/S) scans to produce the full-disk AHI imagery. The instrument is capable of generating full-disk imagery every 10 minutes and performing rapid scan of Japanese and other target areas at 2.5-minute intervals. The spatial resolution varies from 0.5 km to 2 km for different AHI spectral channels. The first AHI images of the Earth were captured on December 18, 2014 and demonstrated a significant increase in spatial and spectral resolutions, compared to the images of its predecessor MTSAT-series satellite which have only one visible and four infrared (IR) channels. With its significantly improved spectral, spatial and temporal resolution and radiance quality, AHI greatly improves the capability of weather forecasting, environmental monitoring, and weather prediction accuracy. It continues to provide valuable data for climate and weather research studies. The AHI data became officially operational on July 7, 2015.

The seventh band (Band #7) of AHI is a Mid-Wavelength IR (MWIR) channel with center wavelength at 3.9-μm and has been designed to monitor temperature variation of low cloud, fire and fog. The spatial resolution for this band is 2 km. The radiometric calibration of these IR bands is performed with the measurements of the internal calibration target of blackbody and deep space. In [1], brightness temperature biases for the AHI IR bands were assessed to meet specification by cross-comparison between the hyper sounders (Aqua/AIRS, Metop-A/IASI, Metop-B/IASI and S-NPP/CrIS) and Himawari-8/AHI.

Earth Observing Systems XXI, edited by James J. Butler, Xiaoxiong (Jack) Xiong, Xingfa Gu, Proc. of SPIE
Vol. 9972, 99720R · © 2016 SPIE · CCC code: 0277-786X/16/$18 · doi: 10.1117/12.2237052

It has been observed that there are stray light appearing in the AHI 3.9-micron channel full disk imagery over a few weeks around February and October-November. These stray light moves with the solar position along both the N/S and E/W directions. In this paper, we quantitatively characterize the AHI stray light.

The AHI instrument has very similar optical design as the Advanced Baseline Imager (ABI) onboard the American GOES-R satellite, which is currently planned to be launched in late 2016. Therefore, characterization, monitoring and trending the stray light in AHI MWIR imagery support the upcoming work of monitoring stray light in GOES-R ABI. In the following, we first analyze the stray light-contaminated AHI imageries on Nov. 2, 2015 and present typical features of the AHI 3.9-μm channel stray light. Then, we developed peak stray light-based index and clustering-based stray light index to monitor the occurrence, location and magnitude of the AHI 3.9-μm channel stray light. We also show evidence of the solar-origin of the stray light in the AHI MWIR channel using stray light-ratio between two AHI MWIR channels.

2. TYPICAL FEATURES OF THE AHI 3.9-μm CHANNEL STRAY LIGHT

The stray light in the AHI 3.9-μm channel full-disk imagery of Earth are mostly observed over a few weeks during February and October-November each year. Figure 1 shows typical location of Sun relative to Earth in the AHI Fixed Grid Coordinate (FGC) when the stray light appears in the AHI 3.9-μm channel imageries on Nov. 2, 2015. The AHI-FGC is defined as on a plane perpendicular to the direction of the AHI-to-nadir. The X and Y axis of the AHI-FGC is the E/W and N/S angle relative to the AHI nadir, respectively. As shown in Figure 1, Sun is located at ~14.75° south of the AHI nadir and moves from West to East relative to Earth during UT 13:40 to 15:00 on Nov. 2, 2015. This is a typical geometric configuration among Sun-AHI-Earth when stray light appears. In this configuration, Sun and Himawari-8 are located at the opposite side to Earth and the Himawari-8 observes the night side of Earth. Since the sun is below the southern edge of Earth, solar light has direct path to illuminate the AHI instrument even though the AHI observes nighttime Earth. It is noted that the AHI 3.9-μm channel stray light repeats its appearance each time when Sun-AHI-Earth move to the same geometric configuration and the line of sight of Sun is at ~10 to ~20 degrees south of the nadir of the Himawari-8. This suggests that the stray light can be related to the leaking of solar light into the instrument.

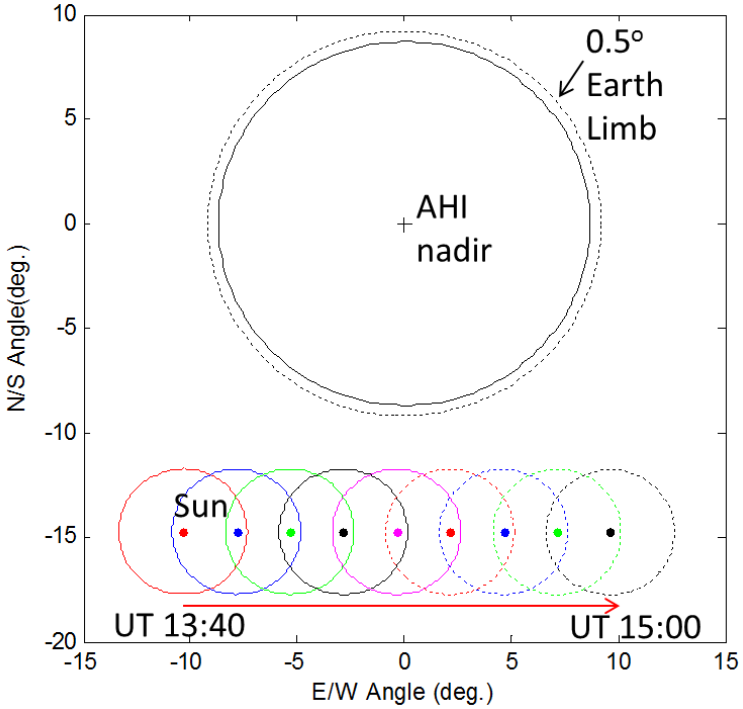

Figure 1: Relative position of Sun to Earth from UT 13:40 to 15:00 on Nov. 2, 2015 projected onto the plane perpendicular to the direction of the AHI-to-nadir, *i.e.* in the AHI-FGC. The X and Y axis are the E/W and N/S angle relative to the AHI nadir, respectively. The solar position is to the south of Earth and marked every 10 minutes with a 3 degree color circle around Sun which appears to move from West to East.

Figure 2 shows three snapshots of the full-disk imagery of Earth observed by the AHI 3.9-μm channel during this period. There are 22 E/W swaths for AHI distributed along the N/S direction with 250 pixels in each swath. Multiple horizontal stripes of stray light can be seen in the northern part of the image. These stray lights are detected by the AHI sensor as additional radiance superimposed onto the Earth scene radiance and move from West to East together with the sun in the AHI-FGC. These stray light stripes are clearly aligned within multiple AHI swaths along the E/W direction.

In order to quantitatively assess and monitor the effects of stray light on AHI imagery products, frame-to-frame difference images between consecutive (10-minute apart) AHI imageries were derived. Figure 3 shows example of frame-to-frame radiance-difference images derived from AHI 3.9-μm channel observations during UT 13:40 to14:30 on Nov. 2, 2015. The horizontal eastward-moving stray light stripes appear as an overlay on the full-disk radiance imagery of Earth scene. Since the amplitude and feature size of these stray light stripes are typically larger than the ten-minute change of Earth scene radiance, the derived frame-to-frame radiance-difference images reveal AHI stray light more clearly. In Figure 3, the horizontal blueish stripes in the upper part of the image are due to stray light in the previous AHI radiance image which has been subtracted. The yellow-reddish stripes to the east are due to stray light in the more recent AHI radiance image.

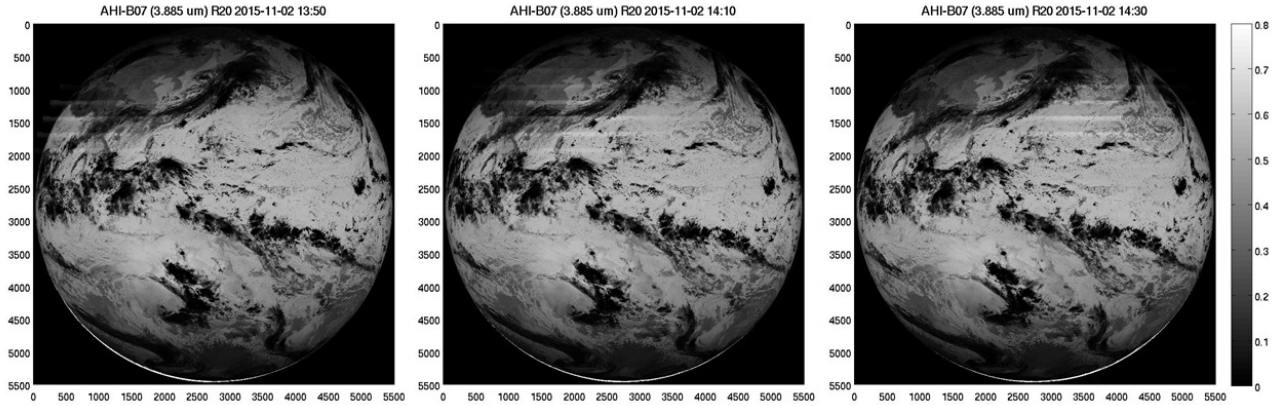

Figure 2: (Left to right) Full-disk imagery of Earth observed by the AHI 3.9 um channel at UT 13:50, 14:10, and 14:30 on Nov. 2, 2015, respectively. The color scale is in radiance (W/m^2-sr-μm).

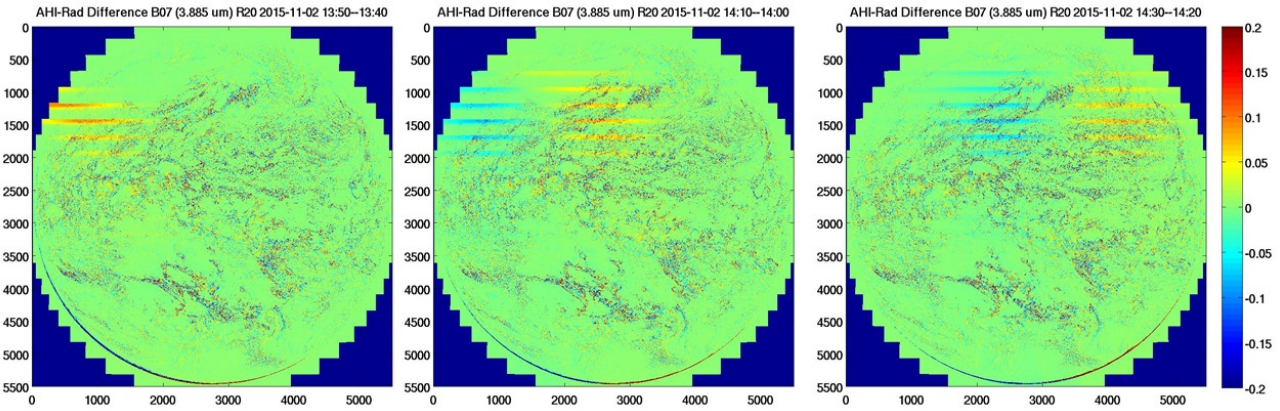

Figure 3: Derived radiance (W/m^2-sr-μm)-difference image between consecutive full-disk imagery from 13:40 to14:30 on Nov. 2, 2015 for the AHI 3.9 um channel.

The difference images shown in Figure 3 can be further processed to quantitatively assess the magnitude of the AHI 3.9-μm channel stray light in terms of radiance and brightness temperature (T_B). Figure 4a-c shows full-disk images of T_B, frame-to-frame radiance-difference and T_B-difference, respectively, derived from AHI observations on Nov. 2, 2015. A region with clear stray light has been identified in the image and marked with a red rectangle. The region spans between pixel #3100 and #3600 along the E/W direction. Figure 4d and 4f shows the mean frame-to-frame radiance difference

and mean scene radiance vs. N/S pixels as derived from averaging pixel values along the E/W direction, respectively. Figure 4e and 4g show the similarly derived mean frame-to-frame T_B-difference and mean scene T_B vs. N/S pixels, respectively.

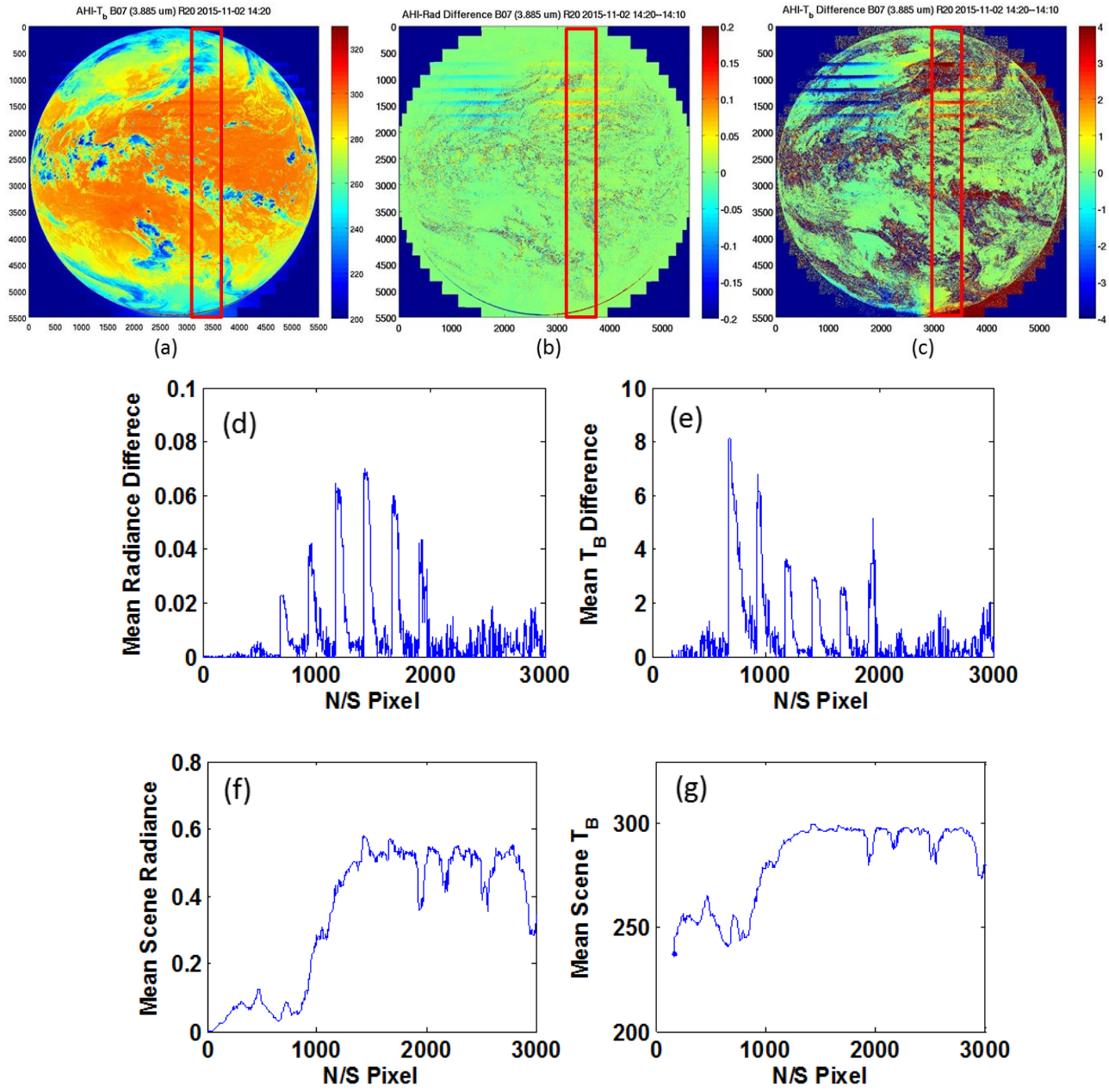

Figure 4: Panel (a-c) shows full-disk images derived from AHI 3.9--μm channel observations on Nov. 2, 2015 for T_B, frame-to-frame radiance-difference and T_B-difference, respectively. The red rectangle in Panel (a-c) illustrated the pixel region for profiling stray light distribution along the N/S direction. Panel (d) and (f) shows the mean frame-to-frame radiance difference and mean scene radiance vs. N/S pixels, respectively. Panel (e) and (g) shows the mean frame-to-frame T_B-difference and mean scene T_B vs. N/S pixels, respectively. Data used for plotting Panels (d-g) are all from consecutive AHI 3.9-μm channel observations at UT 14:10 and 14:20 on Nov. 2, 2015. The mean value is calculated by averaging pixel values between pixel #3100 and #3600 along the E/W direction within the red rectangle shown in Panel (a-c). In this figure, radiance is of unit W/m^2-sr-μm and T_B is of unit K.

From Figure 4d, the AHI 3.9-μm channel stray light can be clearly identified as of saw-tooth pattern with 6 spikes along the N/S direction. Each of these stray light spikes is located within its corresponding AHI swath. The largest stray light spike is located around the N/S pixel #1500 with amplitude as high as 0.07 W/m^2-sr-μm. The amplitude of adjacent stray light spikes decreases as moving away from the swath having the largest stray light spike. On the other hand, the mean Earth scene radiance in Figure 4f shows large variation from < 0.1 W/m^2-sr-μm over cloud to ~ 0.55 W/m^2-sr-μm over typical cloud-free Earth scene. The stray light spikes in Figure 4d are independent of scene radiance value. This further suggests that the stray light is additive to the Earth scene signal observed by the AHI detector. For typical cloud-free Earth scene, the stray light in the AHI 3.9-μm channel can be as large as ~12% of scene radiance.

Figure 4e shows the consequent contamination in brightness temperature for the AHI 3.9-μm channel observation. It can be seen that the deviation of derived brightness temperature from actual value due to stray light can be as high as ~8k over cloud and ~3-4k over typical cloud-free Earth scene. We note that the spike-pattern of T_B-difference in Figure 4e is different from the spike-pattern of radiance difference in Figure 4d. In Figure 4d, the first spike in T_B-difference is of the largest amplitude while the fourth spike in Figure 4e is of the largest radiance-difference due to stray light. This is mainly due to that the stray light is superimposed as additional radiance to the detector. When the scene temperature is low in cloud scene, this additional radiance is translated into a much larger increase in T_B compared to warmer scene.

3. TRENDING AHI 3.9-μm CHANNEL STRAY LIGHT WITH STRAY LIGHT INDEX

3.1 Multiple-day Shift of AHI 3.9-μm Channel Stray light along the North/South Direction

Figure 5a and 5b shows the derived AHI 3.9-μm channel radiance-difference image between UT 14:10 and 14: 20 on Oct. 29 and Nov. 4, 2015, respectively. In Figure 5c, the mean radiance-difference vs. N/S pixel is plotted to show the southward shift of the stray light spikes over six days from Oct. 29 to Nov. 4, 2015. During this period, the solar position moves ~1.915^o from 13.465^o to 15.38^o south of the AHI nadir. The stray light spike pattern is almost maintained in the southward shift. The peak stray light shifts for about 730 pixels, *i.e.* from N/S pixel #936 to #1666, which is estimtaed to have a shift ~1.97^o in the AHI-FGC. The sourthward shift of the AHI stray light over muliple-day is well aligned with the southward movement of the sun in the AHI-FGC.

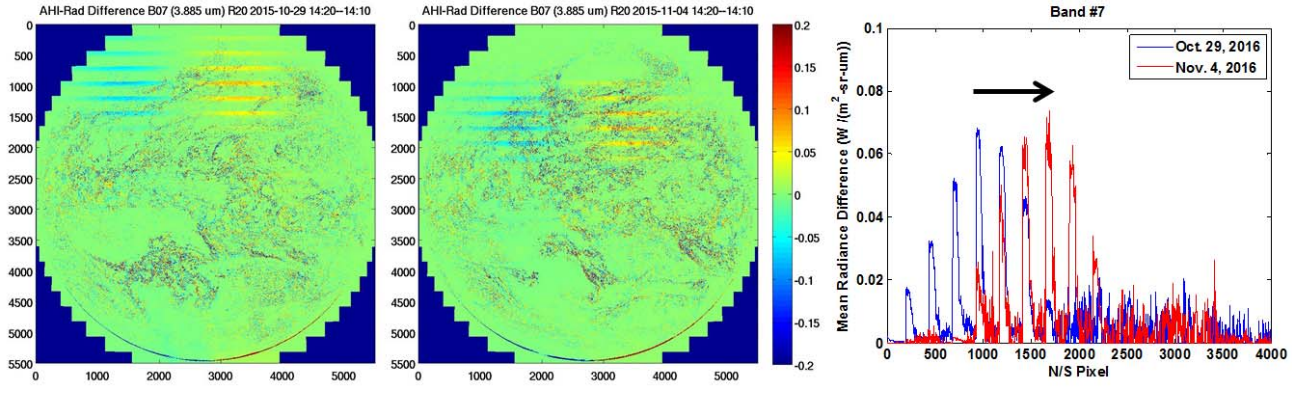

(a) (b) (c)

Figure 5: Panel (a) and (b) show frame-to-frame radiance difference image between UT 14:10 and 14: 20 on Oct. 29 and Nov. 2, 2015, respectively, for the AHI 3.9 um channel. Panel (c) shows the mean radiance difference along the N/S direction as derived from Panel (a-b). The region used for calculating mean radiance difference is the same as the red rectangle shown in Figure 4a-c.

From analysis in Section 2 and 3.1, a few considerations on developing stray light indices to trend the AHI 3.9-μm channel stray light can be summarized as following.

(1) The AHI stray light is superimposed onto the Earth scene signal. Therefore, frame-to-frame radiance difference image is more suitable for characterizing and trending the AHI 3.9-μm channel stray light.

(2) The AHI stray light affect multiple swaths in the AHI imagery, and these stray light move with Sun along both the E/W direction during local night and the N/S direction over multiple days. To monitor the AHI

stray light, we need to be able to identify the stray light-contaminated swaths, i.e. the E/S and N/S pixel or AHI-FGC location of the peak stray light within each swath.

(3) The stray light index also needs to monitor the magnitude of stray light within the stray light-contaminated AHI swaths.

In sections 3.2 and 3.3, we developed indices such as AHI Peak Stray light Index (PSI) and Clustering-based Stray light Index (CSI) to monitor the AHI 3.9-μm channel stray light.

3.2 Monitoring the AHI 3.9-μm Channel Stray light with Peak Stray light Index (PSI)

Using the PSI, we can identify the images contaminated by stray light and monitor the location and radiance-amplitude of the highest stray light within each image. It provides an overall assessment of the stray light performance in the AHI 3.9-μm channel imageries. To do so, we need to first identify stray light in the radiance-difference map. The AHI 3.9-μm channel stray light spans significant extent along the E/W direction within its corresponding swath. By defining the E/W direction as along the X axis and the N/S direction as along the Y axis, we perform a sliding-window averaging to calculate mean radiance $\bar{L}(x) = \frac{1}{101}\sum_{x-50}^{x+50} L(x)$ centered at pixel #x. Next, we find pixels (x, y) such that all values within x-250 to x+250 have $\bar{L}(x) > 0.05$ W/m^2-sr-μm. In this way, the stray light pixels with large extent along the E/W direction can be auickly identified and the isolated pixels with sporadic high radiance-difference values are screened out. After identifying the pixels with stray light contamination, we then define the pixel with the largest mean radiance-difference as the pixel with the peak stray light within the image.

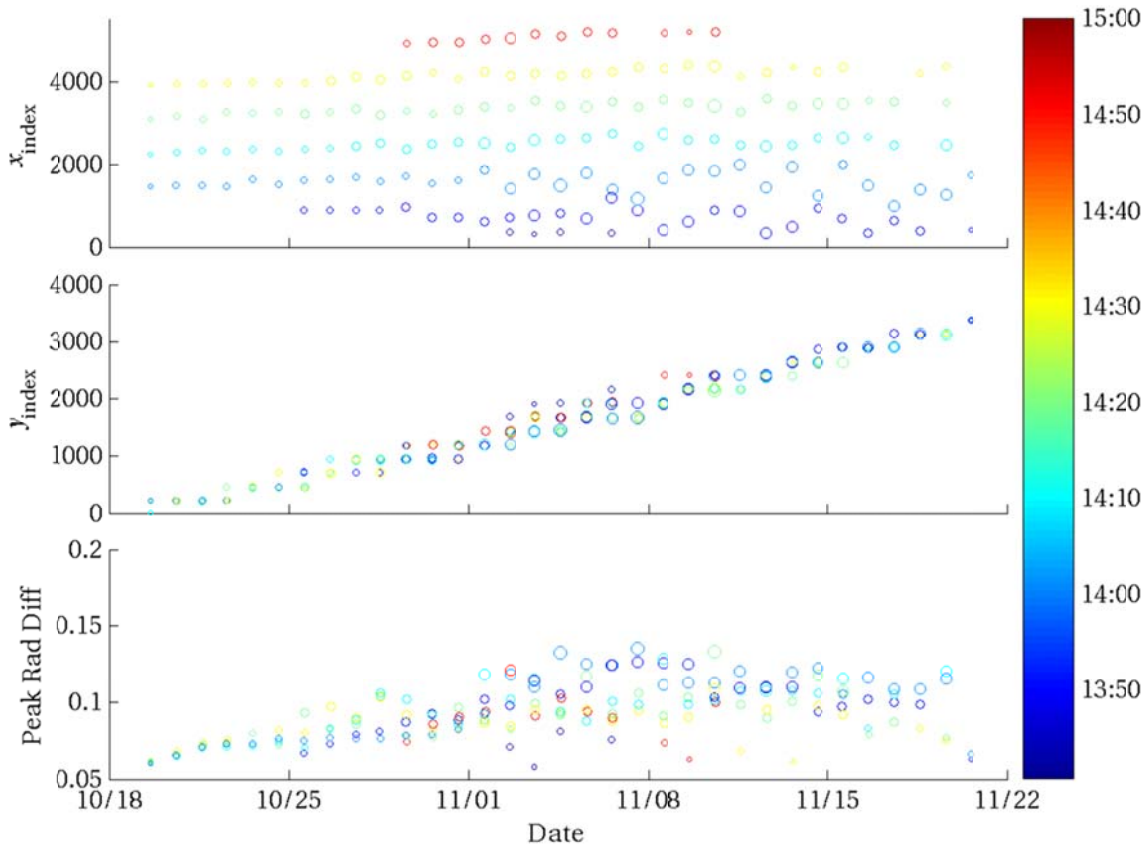

Figure 6: Top and Middle panels show time series of E/W and N/S location of pixel with the peak stray light in each stray light-contanimated image as identified with the PSI method. The circle size indicates the magnitude of the peak stray light. The circle color corresponds to the occurrence time of the stray light as indicated in the color bar to the right. The bottom panel shows the trending of peak stray light magnitude in term of radiance (W/m^2-sr-μm).

Figure 6 shows the trending of location and amplitude of the AHI 3.9-μm channel stray light peak with the PSI method. The first two panels show the E/W and N/S pixel location of the peak AHI stray light. During each day, the locations of the peak stray light move eastward over several images. It is found that the stray light first appears in the AHI imageries on Oct. 19 with four images contaminated. Then, the number of stray light-contaminated images increased to 7 around Nov. 5. After that, the number of stray light-contaminated images during each day decreases until there is no stray light contamination on Nov. 22. From Oct. 19 to Nov. 21, the N/S locations of the peak stray light move from pixel #nearly 0 to pixel #3000. The color-coding and size of the circles in Figure 6 also show the occurrence time and magnitude of the peak stray light. Usually, the peak stray light around UT14:00 have larger amplitude than at other times. From the bottom panel in Figure 6, it can be seen that the peak stray light magnitude increased since Oct. 19, reached as large as 0.13 W/m^2-sr-μm on Nov. 5, then decreased until its disappearance on Nov. 22.

3.3 Trending the AHI 3.9-μm Channel Stray light Performance with Clustering-based Stray light Index (CSI)

In order to further monitor the location and magnitude of stray light within multiple swaths in each stray light-contaminated image, a CSI method has been developed. Using the CSI method, stray light regions are idenfied as having connected pixels with radiance > 0.025 W/m^2-sr-μm and occupying an area > 0.25 degree^2. Figure 7 shows examples of the stray light clusters identified with the CSI method, which are marked in orange color.

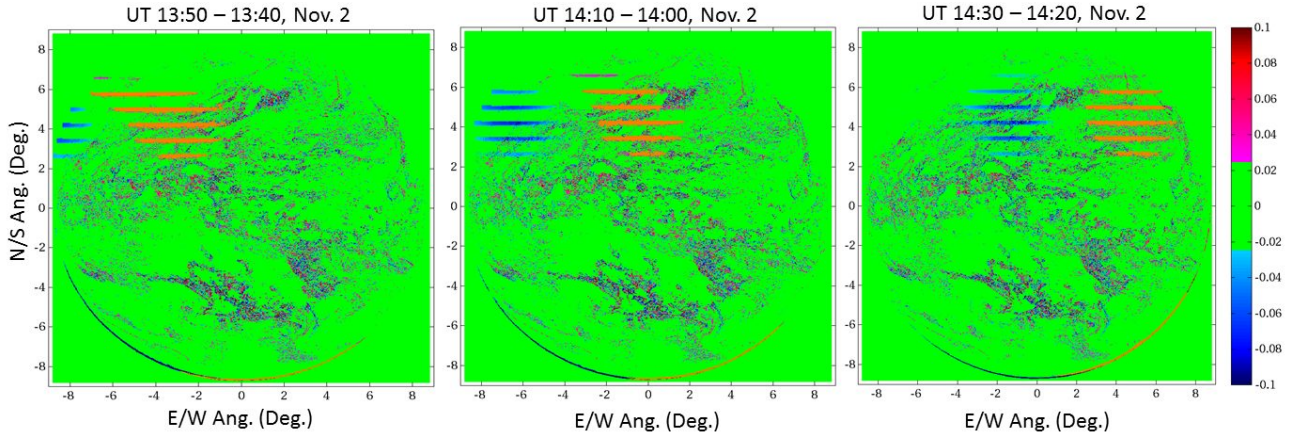

Figure7: Frame-to-frame radiance-difeference images processed with the CSI method over three periods on Nov. 2, 2015. Color scale has been editted to assign green color to pixels with absolute radiance-difference < 0.025 W/m^2-sr-μm. The horizontal and vertical axis are the E/W and N/S angle w.r.t. AHI nadir, respectively, in AHI-FGC. The stray light clusters identified with the CSI method are marked with orange color.

After idenifying the stray light clusters in each contanimated-image, we are able to trend the evolution of the stray light over selected AHI swaths. Figure 8c-e show the trending of the AHI stray light over five selected swaths. The N/S angle locations of the five selected swaths in the AHI-FGC can be idenfied in Figure 8d. Figure 8a-b show the corredsponding solar position in the AHI-FGC when the stralight appears in those five swaths. From Figure 8b and 8d, it can be clearly seen that the appearance time in these swaths and the N/S angular range of the stray light follow the southward solar movement. On the other hand, Figure 8a and 8c show that the E/W angular position of the peak stray light within each selected swath may not be aligned right above the sun, suggesting that the detected stray light have experienced multile reflections. Figure 8e shows the derived mean radiance magnitude of the stray light when passing each selected swath. With the CSI method, we can clearly see that for a given swath, the associated mean stray light magnitude has experienced phases of amplitude-increase, reaching-peak and amplitude-decrease until its disappearnce.

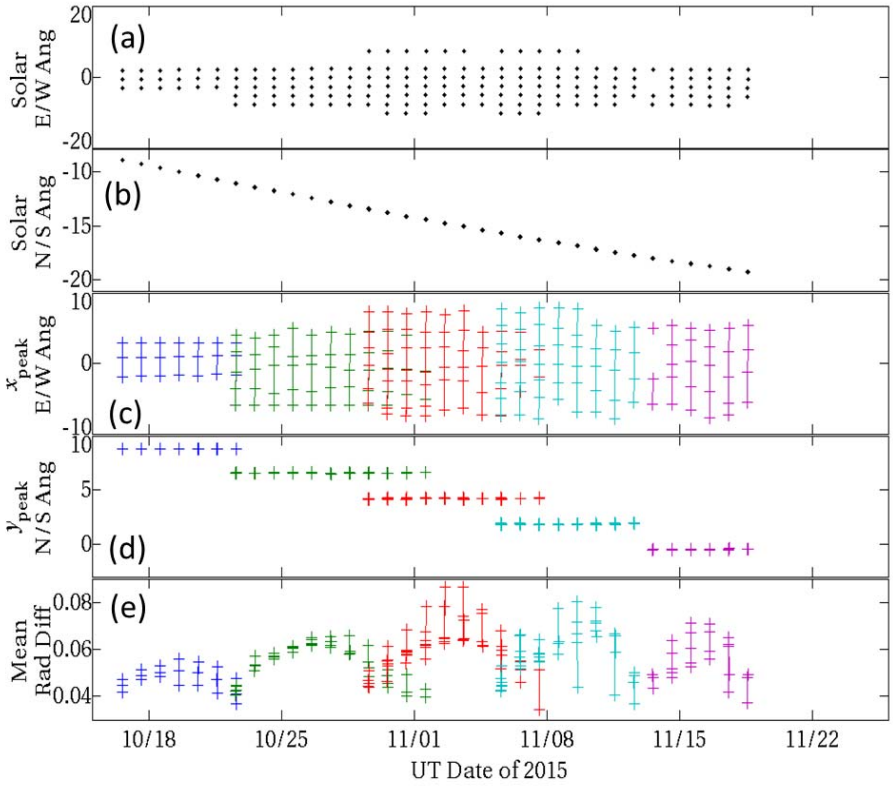

Figure 8: Panel (a) and (b) shows the E/W and N/S angle of the solar position in the AHI-FGC, respectively, when the stray light occured in the five selected swaths within the AHI 3.9-μm channel imageries. Panels (c) and (d) shows the E/W and N/S angular position of the peak stray light in the AHI-FGC, respectively, that appear in the five selected swaths,. Panel (e) shows the trending of the mean frame-to-frame radiance-difference, *i.e.* staylight amplitude, within the stray light clusters overpassing the five selected AHI swaths.

4. SOLAR-ORIGIN OF THE AHI 3.9-μm CHANNEL STRAY LIGHT

Possible causes of the AHI 3.9-μm channel stray light can be due to the direct leaking of the solar light into the instrument after multiple reflections and then detected by the AHI 3.9-μm channel sensor, or due to the thermal emission from the heated thermal body onboard AHI after being illuminated by the solar light. Since the MWIR spectrum of the solar light and heat body emission are quite different, we show here the evidence of direct solar-origin of the stray light with band-ratio of the AHI stray light.

Figure 9 shows the stray light for the AHI Band #7 and Band #8 which was derived similarly as those in Figure 4d. The AHI Band #7 and #8 are both MWIR channel with center wavelength at 3.9 um and 6.2 um, respectively. The stray light in the AHI Band #8 has similar spatial distribution along the N/S direction as that of the AHI Band #7 and the amplitude is much smaller. The right panel further shows scatter plot of the AHI stray light of Band #7 vs. Band #8. The ratio of the stray light magnitude is ~5.2 between these two bands as derived from a linear regression fit.

In Table 1, the ratios of the maximum AHI stray light, solar radiance at Earth, and emission from heat body between these two bands are listed. Both overall ratio (~5.2) and the ratio of maximum magnitude (~5.4) between the AHI Band #7 and #8 stray light are consistent with the ratio of solar radiance (~5.8) at Earth for those two bands. This suggests that the AHI stray light is due to direct illumination by attenuated solar radiation on the AHI detector rather than illumination by onboard thermal body emission due to heating.

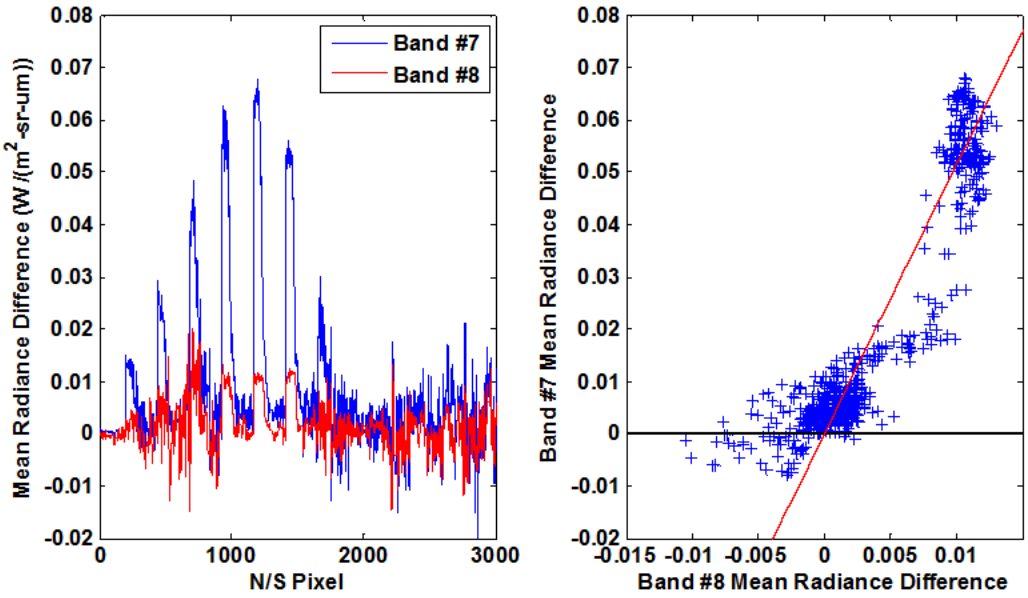

Figure 9: Left: Mean frame-to-frame radiance-difference (stray light) for AHI Band #7 and #8 vs. N/S pixel. The mean frame-to-frame radiance-difference is derived over the stray light-contaminated region as indicated by the red rectangle in Figure 4a-c; Right: Scatter plot of the AHI Band #7 stray light vs. the Band #8 stray light together with the linear regression line in red having a slope of ~5.2. Data between N/S Pixel #820 and #1570 have been used in generating the right panel.

	Center Wavelength (um)	Maximum AHI Stray light Magnitude (W/m^2-sr-μm)	Solar Radiance at Earth (Sun Temperature = 5778k) (W/m^2-sr-μm)	300 K Heat Body Radiation (W/m^2-sr-μm)
AHI Band #7	3.9 um	0.0678	3.2615	0.58578
AHI Band #8	6.2 um	0.0125	0.5589	5.793
Ratio between Band #7 and Band #8		5.42	5.836	0.1

Table 1: Band-ratios of the maximum AHI stray light magnitude, solar radiance at Earth, and 300K heat body radiation calculated between the AHI band #7 and #8.

5. SUMMARY

In this paper, we performed analysis to characterize the AHI 3.9-μm channel stray light. Difference data between consecutive AHI 3.9-μm channel images has been processed to quantitatively characterize and monitor the AHI stray light. The E/W and N/S angular movement of the AHI 3.9-μm channels stray light are aligned with solar movement in AHI-FGC. It is found that the stray light spikes are independent of scene radiance value, which suggests that the stray light is superimposed onto the Earth scene signal observed by the AHI detector. For typical cloud-free Earth scene, the stray light in the AHI 3.9-μm channel can be as large as ~12% of scene radiance. In term of brightness temperature, the deviation of derived T_B from actual value due to stray light can be as high as ~8k over cloud and ~3-4k over typical cloud-free Earth scene. We developed both Peak Stray light-based and Clustering-based Stray light indices, *i.e.* PSI and CSI, to monitor the AHI 3.9-μm channel stray light. We were able to identify the stray light-contaminated swaths, the location of peak stray light within each swath and trend the magnitude of stray light. We also presented the evidence of direct solar origin instead of thermal heating radiation for the stray light through analyzing the stray light ratio between two AHI MWIR bands. The AHI instrument has very similar optical design as the ABI onboard the GOES-R satellite. This work also supports post-launch calibration activities of ABI.

ACKNOWLEDGMENT

The authors would like to thank Japan Meteorological Agency for providing Himawari-8 AHI data and thank for discussion with Changyong Cao, Tung-chang Liu, and Bin Zhang. The manuscript contents are solely the opinions of the authors and do not constitute a statement of policy, decision, or position on behalf of NOAA or the U.S. government.

REFERENCES

[1] Okuyama, Arata, Andou, Akiyoshi, Date, Kenji, Hoasaka, Keita, Mori, Nobutaka, Murata, Hidehiko,Tabata, Tasuku, Takahashi, Masaya, Yoshino, Ryoko and Bessho, Kotaro, "Preliminary validation of Himawari-8/AHI navigation and calibration," *Proc. SPIE 9607*, 96072E (2015).

[2] Griffith, P. "Advanced Himawari Imager (AHI) design and operational flexibility", *6th Asia/Oceania Meteorological Satellite Users' Conference*, Tokyo, Japan, 10 November 2015.

[3] Yu, F. and X. Wu, "Radiometric inter-calibration between Himawari-8 AHI and SNPP VIIRS for the solar reflective channels," *Remote Sensing*, 8(3), 165, (2016).

[4] BESSHO, Kotaro, DATE, Kenji, HAYASHI, Masahiro, IKEDA, Akio, IMAI, Takahito, INOUE, Hidekazu, KUMAGAI, Yukihiro, MIYAKAWA, Takuya, MURATA, Hidehiko, OHNO, Tomoo, OKUYAMA, Arata, OYAMA, Ryo, SASAKI, Yukio, SHIMAZU, Yoshio, SHIMOJI, Kazuki, SUMIDA, Yasuhiko, SUZUKI, Masuo, TANIGUCHI, Hidetaka, TSUCHIYAMA, Hiroaki, UESAWA, Daisaku, YOKOTA, Hironobu and YOSHIDA, Ryo "An introduction to Himawari-8/9 - Japan's new-generation geostationary meteorological satellites," *J. Meteor. Soc. Japan*, 94 (2016).

[5] Yu, F., Wu, Xiangqian, Shao, X. and Kondratovich, V., "Evaluation of Himawari-8 AHI geospatial calibration accuracy using SNPP VIIRS SNO data," *IEEE International Geoscience and Remote Sensing Symposium*, TUP.P32.169, Beijing, (2016).

[6] Shao, X., Cao, Changyong, Zhang, B., Bai, Y., Wu, Xiangqian and Yu, Fangfang, "Comparison of Suomi-NPP VIIRS and HIMAWARI-8 AHI MWIR observations for hot spot and heat island studies," *IEEE International Geoscience and Remote Sensing Symposium*, TU3.L8.4, Beijing, (2016).

[7] Tabata, Tasuku, Andou, Akiyoshi, Bessho, Kotaro, Date, Kenji, Dojo, Ryo, Hosaka, Keita, Mori, Nobutaka, Murata, Hidehiko, Nakayama, Ryuichiro, Okuyama, Arata and Takahashi,Masaya, "Himawari-8/AHI latest performance of navigation and calibration," *Proc. SPIE 9881*, 98812J (2016).